On the fracture behaviour of CFRP bonded joints under mode I loading
Effect of supporting carrier and interface contamination

Heide-Jørgensen, Simon; Teixeira de Freitas, Sofia; Budzik, Michal K.

DOI
10.1016/j.compscitech.2018.03.024

Publication date
2018

Document Version
Accepted author manuscript

Published in
Composites Science and Technology

Citation (APA)
Heide-Jørgensen, S., Teixeira de Freitas, S., & Budzik, M. K. (2018). On the fracture behaviour of CFRP bonded joints under mode I loading: Effect of supporting carrier and interface contamination. *Composites Science and Technology*, *160*, 97-110. https://doi.org/10.1016/j.compscitech.2018.03.024

On the fracture behaviour of CFRP bonded joints under mode I loading: Effect of supporting carrier and interface contamination

Simon Heide-Jørgensen[1], S. Teixeira de Freitas[2,✉], Michal K. Budzik[1,✉]
[1]Aarhus University, Dept. Engineering, Inge Lehmann's Gade 10, 8000, Aarhus C, DK
[2]Delft University of Technology, Fact. Aerospace Engineering, Kluyverweg 1, 2629 HS Delft, The Netherlands

ABSTRACT

This paper addresses the fracture behaviour of bonded composite plates featuring a kissing bond along the crack growth path. Double cantilever beam (DCB) experiments are carried out under a displacement controlled loading condition to acquire the load response. The experimental data are collected and analysed analytically for specimens with and without kissing bond. The following aspects are observed and discussed: effect of the adhesive carrier film, non-smooth crack growth and rising *R* curve. An analytical model taking into account the aforementioned effects is proposed. The kissing bond leads to unstable crack growth resulting in a loss of the load carrying capacity. The presence of the knit carrier in the adhesive film results in the crack growth process characteristic for the stick-slip phenomena and a significant increase of the resistance to fracture of the bondline by triggering a bridging phenomenon. The model shows a very good agreement with the experimental data. A sound understanding of the fracture process is gained enabling analysis and prediction of the effects of kissing bonds and supporting carrier.

Keywords: Bonding; Bridging; Composites; DCB; Kissing bonds; Lattice material; Rising *R* curve

✉ to whom correspondence should be sent (TU Delft): S.TeixeiraDeFreitas@tudelft.nl

✉ to whom correspondence should be sent (AU): mibu@eng.au.dk

1. Introduction

A robust design of layered materials requires a profound understanding of failure phenomena associated with delamination, debonding and interface fracture being the most critical [1]. Evaluation of crack propagation is of central importance for the assessment of failures, the reliability and the damage tolerance of materials and structures [2-4]. Within multilayer materials, bondlines and interfaces are often assumed to be homogeneous. Analytical solutions are proposed for a variety of material systems and fracture modes [5-9]. The cohesive zone framework [10, 11] is successfully adopted, implemented and exploited numerically [12-15]. However, the failure of layered materials can be affected by the presence of local heterogeneities along the crack growth path [16-19]. For composite materials the danger of trapping air, dust, release film or other contamination is high and can lead to premature failure e.g. due to change in the crack front locus [20]. The presence of voids in which no physical bonding between two surfaces exists, could be detected by means of non-destructive methods. However, frequently, the contamination leads to a so-called ‘kissing bond’ where a physical continuity allows for the energy waves to propagate but the mechanical resistance is very low. A considerable number of studies used non-destructive testing methods to address the existence of kissing bonds [21-24]. Contributions addressing the mechanical behaviour of joints containing a kissing bond under mechanical load are less numerous. E.g. in [25] kissing bonds were prepared inside a composite/epoxy adhesive double lap joints. The effects on the load carrying capacity were not investigated. A significant amount of contributions addressing the effect of voids present along an interface, exists. An elasticity method was developed to study the bending and elucidate mechanical properties of laminated panels containing imperfections [26]. An approach utilizing layerwise formulation and representing bondline as an interface with discontinuity of the displacement field was adopted and validated using the finite element method [27]. A multiscale cohesive failure model investigating microheterogeneities was investigated in [28]. The process of decohesion along the imperfect interface was studied within the cohesive zone model framework [29]. In [30], a cohesive zone model was developed to investigate crack growth under the mixed-mode fracture conditions from a circular inclusion. These works indicated a significant effect of the void on the local stress distribution. The Rice and Gao perturbation approach [31, 32] can be used to elucidate fracture properties of the material with the local flaw as well as to deduce the shape of the crack front [33-36]. The perturbation approach was included and further developed to study circular and arbitrary shape inclusions or imperfection bands running parallel to the crack growth direction [17, 35]. An interesting and relevant case could be envisaged once the flaw runs parallel to the crack front through the entire width of the structure. Potentially, the channelling void may turn the steady-state crack growth into an unstable process. In [37] an array of discrete soldered bands was analysed in two dimensions (2D) within the cohesive zone modelling framework. Effects of the crack front plasticity on interactions between the bands were elucidated. Recently, two analytical solutions were proposed for the mode I debonding along an interface with voids [38, 39]. First results suggest a crucial effect of heterogeneities on stability of the crack growth process and the load carrying capacity. These aspects are yet to be investigated for composite materials.

In this work, the effect of a channelling through an interface kissing bond/contamination introduced to the crack growth path on the fracture behaviour of a bonded composite plates is investigated experimentally and analysed theoretically. The bondline consists of an epoxy film adhesive with an embedded polymer carrier resembling a 2D lattice material. Double cantilever beam (DCB) experiments are performed under quasi-static loading conditions. The aim of the study is to characterize the fracture behaviour of composite bonded structures with a kissing bond under mode I opening load.

2. Experimental procedure

2.1. Materials

2.1.1. Composite plates

The Carbon Fibre Reinforced Polymer (CFRP) plates used in this study are manufactured from unidirectional prepreg consisting of the thermoset epoxy resin HexPly 8552 in combination with AS4 carbon fibre (Hexcel Composites, Cambridge, UK). The curing of the composite plates was performed in an autoclave for 120 minutes at $180^{o}C$ and 7 bars pressure. While curing, the surface of the composite plates was in contact with a Fluorinated Ethylene Propylene Copolymer release film (FEP Copolymer A 4000 clear red, Airtech Europe, Niederkorn, Luxembourg). Each plate used for the DCB experiment consisted of a unidirectional CFRP laminate with 10 plies $[0º]_{10}$ resulting in the thickness $h = 1.8 \pm 0.05\, mm$ (the average ± standard deviation). The modulus of elasticity of the plate along the fibre direction $E_1 \cong 100 \pm 10\, GPa$ was evaluated from a series of the three-point bending experiments. In a through-the-thickness direction the value of $E_2 \cong 10\, GPa$ was adopted from [40].

2.1.2. The bondline

The adhesive used for bonding composite plates was in the form of the epoxy film AF163-2K (3M Netherlands B.V., Delft, Netherlands) with a supporting, knitted, carrier. The carrier is used to maintain the thickness of the adhesive bondline while curing. **Fig. 1** (**a**) shows a schematic representation of the adhesive system. The carrier consists of a two-dimensional, diamond-celled lattice knit of nylon fibres of $t = 40 - 50\ \mu m$ diameter. The cured epoxy adhesive is characterized by the Young's modulus $E_a \cong 1.1\ GPa$ and a stress at failure (the epoxy without the carrier) $\sigma_f \cong 48\ MPa$ [40].

2.2. Specimens preparation

2.2.1. Surface pre-treatment and contamination

Prior to bonding the surfaces of the adherends were subjected to a surface pre-treatment consisting of two steps: 1) cleaning with PF-QD solution and 2) UV-ozone treatment. The PF-QD (PT Technologies Europe, Cork, Ireland) is a cleaning solvent for surface cleaning and degreasing [41]. Surfaces were wiped with a cloth soaked with PF-QD. The UV-ozone treatment was performed using an in-house apparatus consisting of $30\ W$ UV-lamps with a sleeve of natural quartz (UV-Technik, Wümbach, Germany) – wave lengths were approximately $184.9\ nm$ and $253.7\ nm$. Samples were treated for 7 minutes at a distance of 40 mm from the UV-lamps [42-45]. After the surface pre-treatment some of samples were contaminated with a band of a 'kissing bond' or a 'weak bond'. The contamination consisted of applying the release agent MARBOTE 227/CEE (Marbocote Ltd, Middlewich, UK). The composite surface was wiped with a cloth impregnated with the release agent and left to dry for 15 minutes. This procedure was repeated six times at the contamination strip area. Weight measurements of samples before and after the contamination showed a contamination weight of approximately $0.12\ \mu g/mm^2$. In a previous study [44], contact angle measurements on composite surfaces with the exact same surface treatment showed an average of $40.9° \pm 5.6°$

angle on the surface after pre-treatment (PF-QD+UV/ozone) and $110.5° \pm 0.7°$ after contamination.

2.2.2. Bonded specimens

DCB coupons were manufactured by bonding two composite plates. The bonding process consisted of a secondary bonding, meaning that the composite plates were bonded after being cured. The bonding curing cycle was performed in an autoclave for 90 minutes at $120^{o}C$ and 3 bars pressure with the contamination strip being applied along ca. $20 - 25\ mm$ of the $220\ mm$ length, on the surface of one of the CFRP adherends. **Fig. 1** (**b**) shows an example of the bonded test panels (with contamination). Five specimens were cut from the bonded panels to the desired dimensions of $25\ mm$ in width and $220\ mm$ in length. Subsequently the adhesive thickness $t = 0.24 \pm 0.04\ mm$ was measured with the optical microscopy – see **Fig. 1** (**c**).

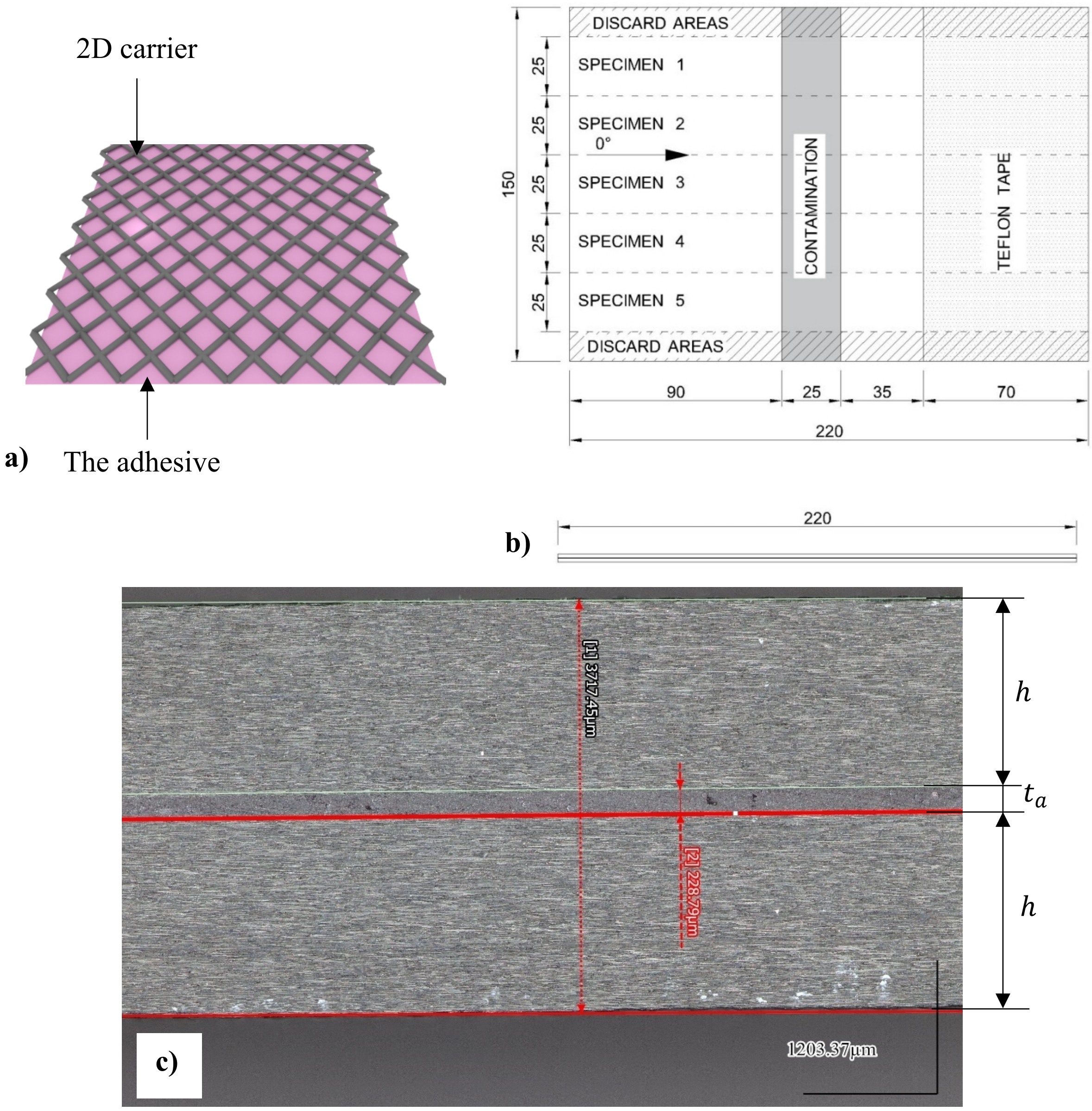

Fig. 1. (**a**) Schematic representation of the adhesive system AF163-2K. (**b**) Bonded composite DCB panel with the contamination strip (dimensions in mm). (**c**) Characteristic dimensions of the composite plate and the bondline.

Fig. **2** shows an example of the ultrasonic C-scan of the contaminated specimens before testing (squirter C-scan, 10 MHz frequency, crystal diameter 10 mm, water nozzle 8 mm diameter, scanned every 1 mm, 10 dB damping, no filters). The Teflon® tape area of the pre-crack is clearly visible, however, a more regular signal could be expected. Due to the wet environment in which the scanning takes place, a water penetration from the free edges is observed at the areas of the Teflon® insert. No defect can be detected in the area of the contamination strip. This confirms the presence of a 'kissing bond' inside DCB specimens.

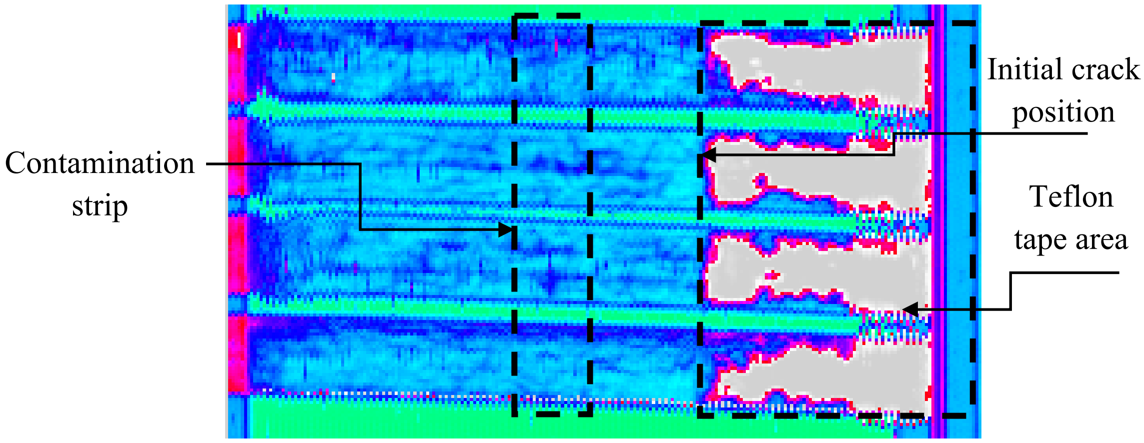

Fig. 2. Ultrasonic C-scan of the contaminated DCB specimens [46].

2.3. DCB test

The experimental configuration is presented in **Fig. 3**. DCB specimens were installed in an universal testing machine (Zwick/Roell Z050, Zwick/Roell, Germany) and tested under displacement rate controlled conditions: $\frac{d\Delta}{dt} = \dot{\Delta} = 10\ mm/min$. The applied force, P, and the specimen tip displacement, 2Δ, were recorded simultaneously at $10\ Hz$ acquisition rate and used for the data reduction.

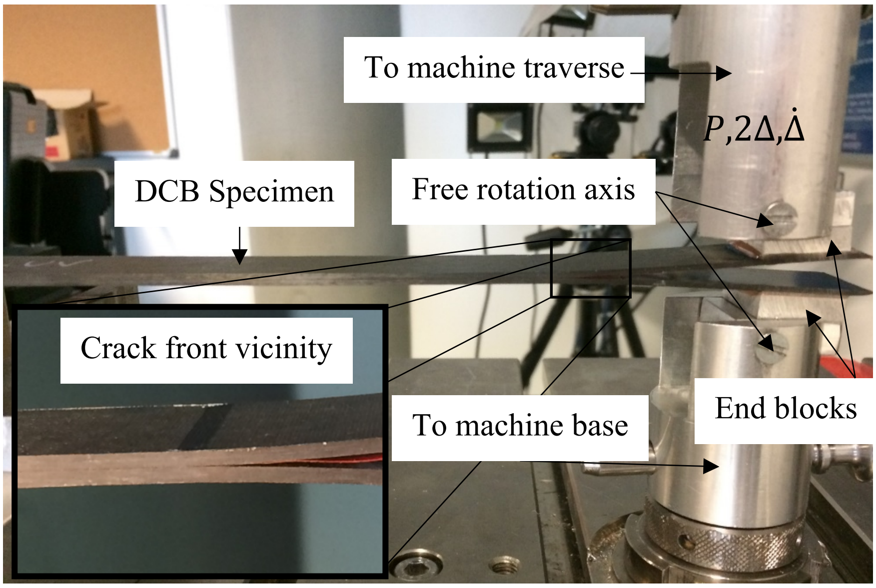

Fig. 3. The DCB experiment.

2.4. In-situ and post-mortem observations

The crack growth process was tracked from the side using a 5 megapixel resolution optical macro/microscope (Dino, ProLite, The Netherlands) at $1Hz$ acquisition rate. To investigate features of fracture surfaces a wide area, three-dimensional measuring macroscope and a fringe projection scanner (Keyence VR-3200, Japan) were used. The scanner is characterized by $< 100\ nm$ out-of-the-plane resolution with up to a $200x200\ mm^2$ measuring area.

3. Analytical model

It is postulated that the composition of the bondline i.e. the epoxy adhesive and the 2D grid, requires an analytical model to be decomposed accordingly.

3.1. Steady-state model of debonding

The physical model is based on the kinematic assumptions of simple beam theory, e.g. in which the effects of the shear forces (thickness $h << a$, with a being the instantaneous crack length) are neglected. Considering half of the symmetric specimen (from the boundary condition at the loaded tip) the compliance of the specimen read as:

$$C = \frac{\Delta}{P} = \frac{a^3}{3E_1 I} \tag{1}$$

where $I = \frac{bh^3}{12}$ is the second moment of the beam cross section area. The product $E_1 I$ expresses the effective bending rigidity assuming cylindrical bending of the laminated plate [47]. Using the Irwin-Kies compliance formula [2], the mode I Energy Release Rate (ERR), i.e. the driving force, can be expressed as:

$$\mathcal{G}_I = \frac{P^2 dC}{2b da} \tag{2}$$

The effect of the finite compliance of the loading system is in the present case neglected. Substituting eq. (1) into eq. (2) yields:

$$\mathcal{G}_I = 3\frac{P}{bh}\sqrt[3]{\frac{P\Delta^2}{2bE_1}} = \frac{1}{6E_1 h^3}\left(\frac{Pa}{b}\right)^2 \tag{3}$$

The Griffith's fracture criterion is assumed once the driving force equals the fracture energy $\mathcal{G}_I = \mathcal{G}_{Ic}$, denoting the onset of the crack. Assuming $\mathcal{G}_{Ic} = const.$ eq. (3) is solved for a and introduced to eq. (1) revealing that at the crack onset, the linear relation between P and Δ bifurcates into a nonlinear one:

$$P = \gamma\,\Delta^{-1/2} \tag{4}$$

with $\gamma = 2b\sqrt[4]{\frac{h^3}{6}E_1\,\mathcal{G}_{Ic}}^{\,3/4}$. Eq. (4) provides a power law for the steady-state, self-similar crack growth process and can be conveniently used to extract the fracture energy by a simple allometric function curve fitting. Interchanging the dependent variable in eq. (3) through eq. (1), viz. $P \rightarrow \Delta$, and upon further rearrangement the instantaneous crack length is given by:

$$a = \left(\frac{3E_1h^3}{8\,\mathcal{G}_{Ic}}\right)^{\frac{1}{4}}\Delta^{\frac{1}{2}} \tag{5}$$

The second scaling is revealed - during the DCB experiment the crack position $\sim\Delta^{\frac{1}{2}}$. We introduce the crack growth rate in the form:

$$\dot{a} = \frac{da}{dt} = \frac{\partial a d\Delta}{\partial\Delta dt} = \frac{1}{2}\left(\frac{3E_1h^3}{8\,\mathcal{G}_{Ic}}\right)^{\frac{1}{4}}\dot{\Delta}\Delta^{-\frac{1}{2}} \tag{6}$$

Eq. (6) seems of fundamental importance revealing an inherent effect of crack growth and loading rates on the fracture energy, $\mathcal{G}_{Ic} \sim \left(\frac{\dot{\Delta}}{\dot{a}}\right)^4$. The elastic strain energy is given by $U = \frac{1}{2}P\Delta = \frac{1}{2} C^{-1}\Delta^2$. The rate form of U can be obtained by using the chain rule:

$$\frac{dU}{dt} = \frac{\partial U}{\partial \Delta}\frac{d\Delta}{dt} + \frac{\partial U}{\partial a}\frac{da}{dt} \tag{7}$$

With $U = \frac{3}{4}\frac{E_1 I \Delta^2}{a^3}$:

$$\dot{U} = \frac{3}{2}E_1 I\left(\frac{2\dot{\Delta}\Delta}{a^3} - \frac{3\Delta^2\dot{a}}{a^4}\right) \tag{8}$$

where $\dot{U} = \frac{dU}{dt}$. Under the displacement controlled conditions $\mathcal{G}_I \stackrel{\text{def}}{=} -\frac{1}{b}\frac{dU}{da}$ yielding:

$$\mathcal{G}_I = \frac{1}{b}\left(\frac{\partial U}{\partial a} - \frac{\partial U}{\partial \Delta}\frac{d\Delta}{da}\right) \tag{9}$$

leading to:

$$\mathcal{G}_I = E_1\, h^3\left[\left(\frac{3\Delta^2}{8a^4}\right) - \left(\frac{1}{4}\frac{\Delta\,\dot{\Delta}}{a^3\dot{a}}\right)\right] = \mathcal{G}_{Is} - \mathcal{G}_{Ik}(\dot{\Delta},\dot{a}) \tag{10}$$

The result, with $\mathcal{G}_{Is}$ being the static part and $\mathcal{G}_{Ik} = f(\dot{\Delta},\dot{a})$ being the kinetic part, refers to the generalization of the Griffith's fracture theory [48, 49]. Simplifying eq. (5) to a more convenient form:

$$a = \psi \Delta^{\frac{1}{2}} \tag{11}$$

with $\psi = \left(\frac{3E_1 h^3}{8\ \mathcal{G}_{Ic}}\right)^{\frac{1}{4}}$, subsequently, taking the power of 2 on both sides and upon further derivation yields:

$$\frac{d\Delta}{da} = 2\psi^{-2} a \tag{12}$$

which upon substitution to eq. (9) leads to an alternative form of eq. (10):

$$\mathcal{G}_I = \frac{E_1 I}{b}\left[\left(\frac{9\Delta^2}{2a^4}\right) - \left(6\frac{\Delta}{a^2}\psi^{-2}\right)\right] \tag{13}$$

Eq. (13) exposes an inherent property of the DCB set-up for which the driving force is expected to rise during the experiment with the asymptote of a quasi-static fracture energy $\mathcal{G}_{Ic}$. As such, the recorded experimentally measured $\mathcal{G}_I$, though directly related, cannot be treated as the intrinsic material property. While, quantitatively, the effect is not expected as dominating (for the present case the ratio $\frac{\mathcal{G}_{Ik}}{\mathcal{G}_I}$ is evaluated to $\max. 10\%$) it highly affects qualitative interpretation. Following the 'standard' analysis, $\mathcal{G}_I = \mathcal{G}_{Is}$ viz. eq. (3), once $\mathcal{G}_I = \mathcal{G}_{Ic}$, the crack growth is essentially a 'critical state' process viz. $\frac{d\mathcal{G}_I}{da} = 0$. During the DCB experiment, the presence of the kinetic component, $\mathcal{G}_I = \mathcal{G}_{Is} - \mathcal{G}_{Ik}$ viz. eq. (10) indicates the process to be stable:

$\frac{d\mathcal{G}_I}{da} > 0$ and $\frac{d^2\mathcal{G}_I}{da^2} < 0$ and may explain the reason behind a rising resistance curve as often observed when testing layered materials [50, 51].

3.2. Non-smooth debonding

The core of the analytical model is shared with the one used in [39] and, thus, some details are omitted in the following presentation. A cantilever beam is attached to a unit pattern model at the crack tip following **Fig. 4**.

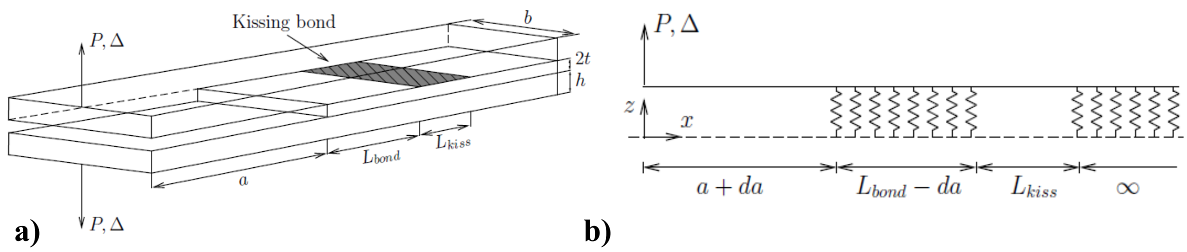

Fig. 4. The model of the beam on interface with the kissing bond. **a**) Illustration of the DCB specimen with a kissing bond. **b**) Schematics of the kissing bond model

The governing equation of the Euler-Bernoulli beam, following Pagano's model, [5], reads:

$$E_1 I \frac{d^4 w}{dx^4} + b\sigma(x) = 0 \tag{14}$$

where σ represents the cohesive stress inside the bondline. $\sigma = 0$ for the unbonded zone(s) and $\sigma \neq 0$ for the bonded zones. Due to the finite rigidity of the interface a process zone of length $\lambda^{-1} = \sqrt[4]{\frac{4E_1 I}{k}}$ exists ahead of the crack tip for which the $\sigma(x) > 0$. Since $\frac{E_a}{E_2} = \frac{1.1}{10}$ the foundation constant k will be associated solely to the bondline material, i.e. $k = m\left(\frac{E_a}{t}\right)b$, where m allows for an arbitrary interpretation of the crack front stress state [52, 53]. In the present case, the plane strain conditions are assumed at the crack tip [54] leading to $\lambda^{-1} \cong 2.4\ mm$. The model can be extended to account for the cohesive tractions exhibited by the composite plate [52]. In this case, the foundation modulus needs to be redefined as $k_t^{-1} = k^{-1} + k_C^{-1}$ with k_C^{-1} reflecting the transverse stiffness of the composite material. The model is then subdivided into a free part (cantilever), a first bonded zone of length L_{bond}, a kissing bond zone of length L_{kiss}, and a second bonded zone spreading to infinity. The region from the first to the second bonded zone constitutes the unit pattern which can be incorporated as a loop used repeatedly during the crack growth. The solution for each of the governing equations give the full description of the unit pattern model:

$$w(x,\beta) = \begin{cases} \dfrac{P\left(\frac{1}{2}L\beta x^2 + \frac{1}{2}a x^2 - \frac{1}{6}x^3\right)}{E_1 I} + C_1 x + C_2 & \forall\ 0 \le x \le a + da \\ \cosh(\lambda x)\left(C_3 \cos(\lambda x) + C_4 \sin(\lambda x)\right) + \sinh(\lambda x)\left(C_5 \cos(\lambda x) + C_6 \sin(\lambda x)\right) & \forall\ a + da \le x \le a + L_{bond} \\ \frac{1}{6}C_7 x^3 + \frac{1}{2}C_8 x^2 + C_9 x + C_{10} & \forall\ a + L_{bond} \le x \le a + L_{bond} + L_{kiss} \\ e^{\lambda x}\left(C_{11}\cos(\lambda x) + C_{12}\sin(\lambda x)\right) & \forall\ a + L_{bond} + L_{kiss} \le x \le \infty \end{cases} \tag{15}$$

where $C_1, C_2, C_3, C_4, C_5, C_6, C_7, C_8, C_9, C_{10}, C_{11}, C_{12}$ are unknown constants to be determined through the four boundary conditions, i.e. $w(x=0)=\Delta; \frac{d^2w}{dx^2}(x=0)=0 \wedge w(x=\infty)=0; \frac{dw}{dx}(x=\infty)=0$, and C^3 continuity conditions (continuity of displacement field, rotation, strain and shear forces) between each of the zones. In this model a is the initial crack length, da is the instantaneous crack growth and β is the ratio defined as $\beta = \frac{L_{bond}}{L_{kiss} + L_{bond}}$. Importantly, in the far field the solution experiences exponentially modulated decay while within the zone of the finite length ($\cong 2\lambda^{-1}$) exponential growth toward the ends could be expected [52, 55]. The model is implemented through a script written in Matlab® (v.2016b, MathWorks, USA) in which the continuous loading conditions are reproduced and the snap-back behaviour, viz. $d\Delta < 0$, is penalized. The ERR is then obtained through eq. (9).

3.3. Bridging

The bridging phenomena is considered an efficient way of increasing the fracture energy of composite materials. Different models are proposed to account for the fibre bridging between the cracked surfaces [6, 56-59]. Since, in the present case, the composite adherends are bonded the bridging is not expected once the crack locus is cohesive within the bondline, i.e. the bridging due to the fibres closing the cracked faces is an unlikely event. However, the physical composition of the bondline, i.e. the adhesive and the polymer carrier induces a bridging component between the two bonded surfaces which proved an efficient way of increasing the total ERR defined as:

$$\mathcal{G}_{It} = \mathcal{G}_I + \mathcal{G}_b \tag{16}$$

where $\mathcal{G}_I$ refers to the ERR from eq. (13) and $\mathcal{G}_b$ is the ERR due to bridging. In the present case, the bridging will 'effectively' be defined by:

$$\mathcal{G}_b = \frac{\mathcal{G}_{cp}}{b} \int_{a_0}^{a_0 + l_{bz}} f(a) da \tag{17}$$

where $\mathcal{G}_{cp}$ is the energy at failure associated with the carrier (at this stage we will not decide the failure mode of the carrier) viz. a constant, which can be deduced from the experimental data. a_0 is the crack length at which the bridging phenomenon begins (most likely the initial crack length) and l_{bz} is a self-similar length of the bridging zone evaluated from the experimental data once the steady-state process begins. The definite integral formulation accounts for a cumulative effect from increasing the length of bridging zone during the crack growth. In general, an arbitrary, non-dimensional, function $f(a)$ of the crack position can be used as a kernel of the integral. In the present case $f(a)$ is assumed a constant, and thus, $\mathcal{G}_b$ increase linearly until the full length of the bridging zone is established, $\mathcal{G}_b \sim \int_{a_0}^{a_0 + l_{bz}} 1 da \cong l_{bz}(a)$. From that moment, l_{bz} is treated as an inherent property related to the bridging phenomena and further increase of the crack length will result in a steady-state process for which $l_{bz} = const. \therefore \frac{d\mathcal{G}_b}{da} = 0$. Equivalently, at the front of the bridging zone the carrier film needs to fracture or peel from the adherend. Finally, once the distance between the crack tip and the kissing bond $< l_{bz}$, l_{bz} decreases and so will be $\mathcal{G}_b$ as stated by eq. (17). The effect of the formation and the diminishment of the bridging zone on the ERR can be described as follows:

$$\mathcal{G}_b = 0 \ \forall \ a \leq a_0 \qquad (18)$$

$$\frac{d\mathcal{G}_b}{da} > 0 \ \forall \ a \to a_0 + l_{bz}$$

$$\frac{d\mathcal{G}_b}{da} = 0 \ \vdash \ \mathcal{G}_b = const. \wedge l_{bz} = const.$$

$$\frac{d\mathcal{G}_b}{da} < 0 \ \forall \ l_{bz} > l - a$$

where l is the distance between the load application point and the end of the bonded zone. Within the scope of the present study the fracture energy of the kissing bond region was not evaluated. It is deemed (though not verified) that within this region the bonding is mainly due to very weak van der Waals interactions. Specimens with a (full) kissing bond pre-treatment felt apart under handling. Therefore, within the kissing bonds, values of $k = 0$ and $\mathcal{G}_{Ic} = 0$ were adopted when necessary.

4. Results and Discussion

4.1. Continuous interface

In **Fig**. **5** the load response during debonding of composite plates is presented. Results correspond to specimens with continuous interfaces – without the kissing bond. The experimental (points) and the analytical (lines) data corresponding to the steady-state model are presented. The analytical data provides the initial compliance of the system, eq. (1) (black line and a shaded area representing 95% confidence bounds) and the crack growth path, eq. (4) (red line with the shaded area referring to 95% confidence bounds).

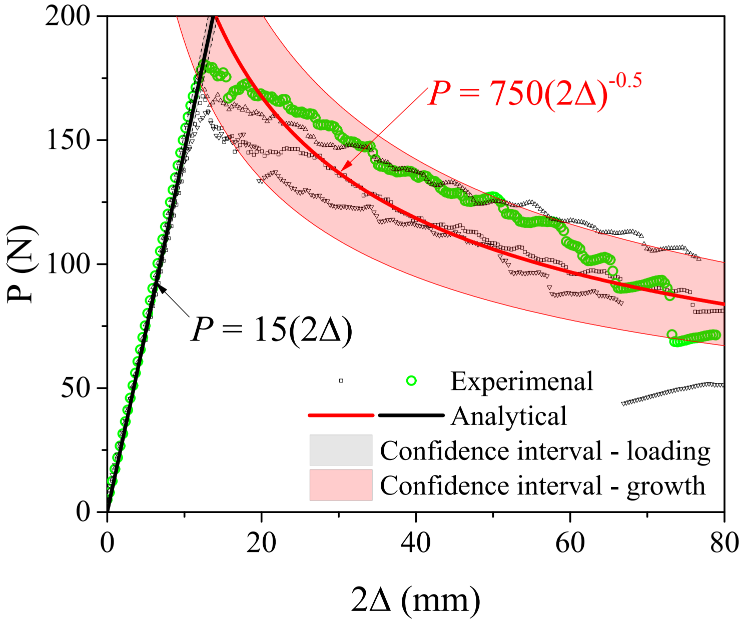

Fig. 5. The load response curves for the specimens without kissing bond. The experimental and the analytical data are plotted with the 95% confidence bounds.

During loading the experimental and the analytical data exhibit a similar, linearly increasing trend. The agreement is very good. Once the fracture threshold is attained, i.e. $\mathcal{G}_I = \mathcal{G}_{Ic}$, the linear path bifurcates to a nonlinear one and $P \sim \Delta^{-0.5}$. The crack growth stage begins. The analytical curve characterizing this stage is obtained by fitting an allometric function with the fixed power coefficient of -0.5 to all the experimental data. The coefficient of determination obtained $R^2 \cong 0.95$, suggests a very good correlation between the analytical and experimental data, however, a clear, systematic, deviation can be noticed. To facilitate this observation one of the experimental series is highlighted. In specific, the onset of the crack growth, as indicated by the experimental data, initiates from the analytical lower bound and tends, almost linearly, to the upper bound. This indicates a rising trend of the R curve. In the final stage, the trend is reversed and the curve begins to move towards the lower bound. The crack front is approaching the end of the crack growth path, which remains out of the scope of the present study. The more detailed analysis of this behaviour can be found in [52, 60].

4.1.1. Crack locus and crack growth path

Fig. **6** shows details of the crack growth process (**a**) and a representative microscopic view of the fracture surface presenting a unit cell of the carrier (**b**).

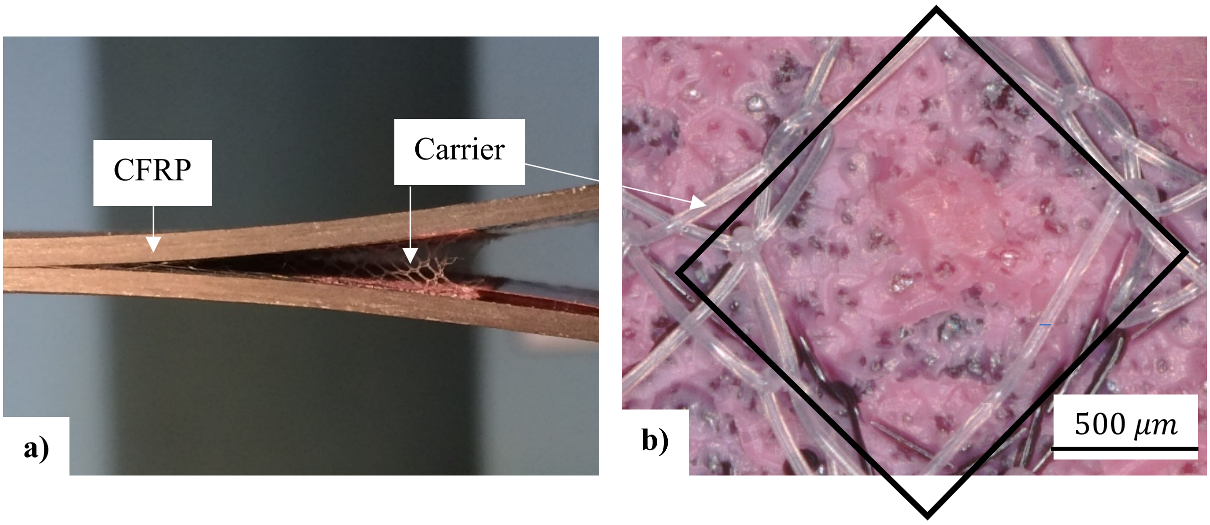

Fig. 6. Bridging of the cracked faces due to the embedded net. (**a**) An image taken during the DCB experiment. (**b**) A microscopic view of the fracture surface with the characteristic diamond-celled feature of the embedded net.

From **Fig**. **6** (**a**) it is apparent that the crack growth is hindered by the bridging phenomena introduced by the knit carrier of the adhesive. Importantly, the crack growth is of cohesive nature, i.e. within the adhesive material, for all the specimens tested. The appearance of the fracture surface is presented in **Fig**. **6** (**b**) where the (pink) epoxy phase coexists with the knitted structure of the carrier.

In **Fig. 7** a three-dimensional (3D) representation of the fracture surface is presented. In **Fig. 7** (**a**) the crack growth paths for both of the specimen adherends (denoted by + and -) are shown. In **Fig. 7** (**b**) and (**c**) a more detailed view of an arbitrary region of the crack growth path is presented.

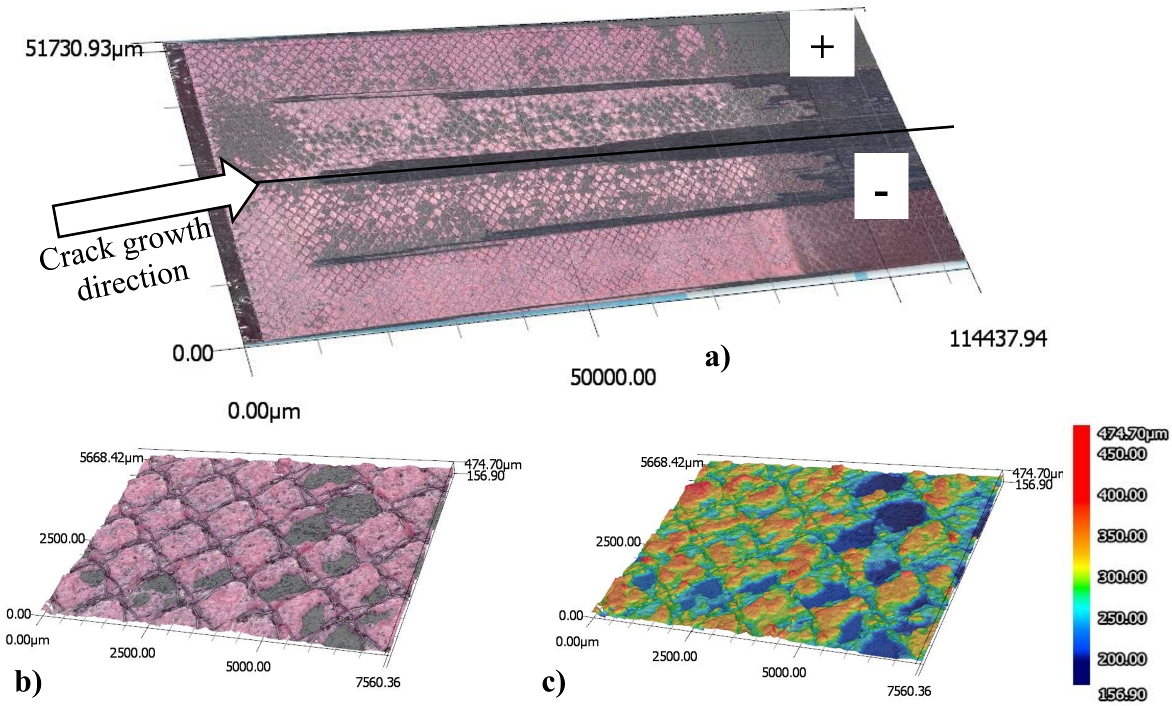

Fig. 7. Details of the fracture surfaces obtained by a scanning microscope. (**a**) Optical scan of the entire fracture surface for both adherends (+ and -). (**b**) Optical and magnified view of the fracture surface with visible features of the embedded net. (**c**) A 3D representation of (**b**). The scale is given in μm.

The fractography reveals a specific pattern of the carrier grid. It is becoming evident that two fracture processes take place simultaneously. At first, the crack grows inside the epoxy phase. The crack tip does not propagate through the filament phase c.f. **Fig. 6** (**b**), instead it propagates along the interface between the epoxy and the carrier grid. Consider following scenarios: 1) the carrier remains bonded to one of the adherends as the crack propagates cohesively, and 2) the carrier remains attached to both adherends. In the first case, the entire process of crack growth is driven by the epoxy phase. The presence of the carrier is affecting the composition of the crack growth path, however such effect is expected to be relatively small (this will be followed at the later stage). The latter case, depicted in **Fig**. **6** (**a**), is found for most of the specimens tested and enables the bridging between two adherends. The additional, unexpected, dissipation process functionalized through the bridging can, potentially, severely affect the strain energy release process.

4.1.2. Driving force and resistance curves

In **Fig**. **8** the driving force/resistance curves are plotted. Results of three experiments, $\mathcal{G}_I^{exp}$, are plotted as points. The analytical results are presented as lines - dashed and solid. Plotted are: the total ERR, $\mathcal{G}_{It}$ c.f. eq. (16), together with the bridging, $\mathcal{G}_b$ c.f. eq. (17) and the static, $\mathcal{G}_{Is}$, and the kinetic, $\mathcal{G}_{Ik}$ components of $\mathcal{G}_I$ c.f. eq. (10).

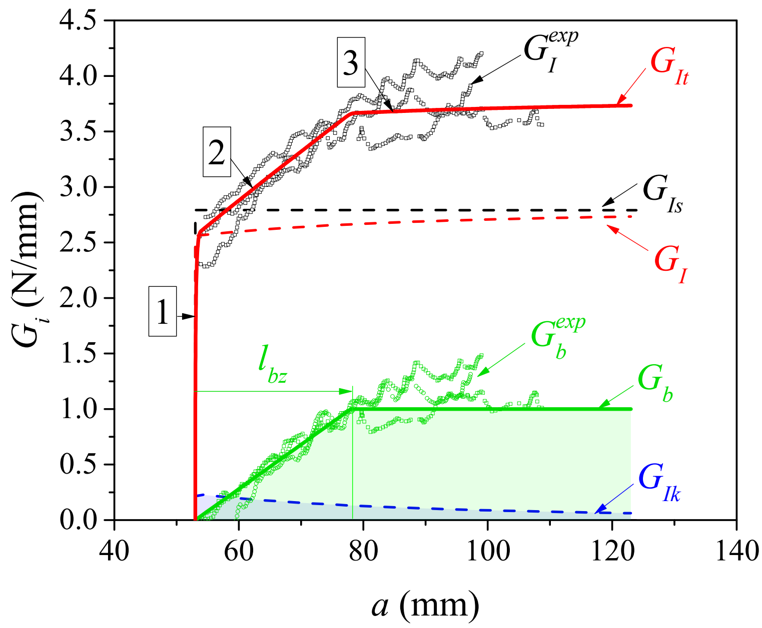

Fig. 8. The driving force/resistance curves. The experimental and the analytical results are plotted. $\mathcal{G}_I^{exp}$and $\mathcal{G}_b^{exp}$ represents the total and the bridging component of ERR obtained from the experimental data. The analytical, total ERR $\mathcal{G}_{Itot}$ is composed from static $\mathcal{G}_{Ist}$, kinetic $\mathcal{G}_{Ik}$ and bridging $\mathcal{G}_b$ components.

To facilitate the discussion a schematic representation of the fracture process is provided in **Fig. 9**.

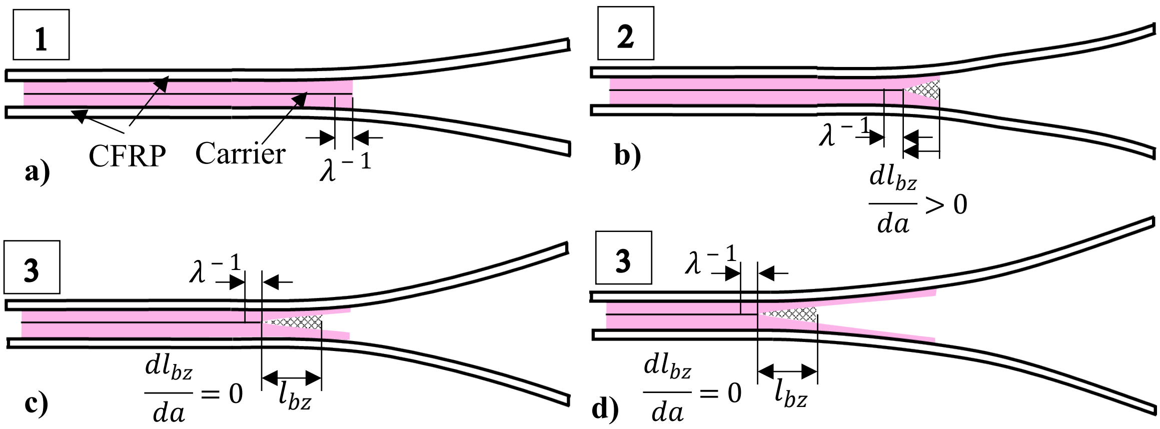

Fig. 9. Proposed description of the fracture process. (**a**) The configuration at the crack onset. (**b**) The crack growth through the bondline is assisted by creation of a bridging zone. (**c**)→(**d**) The bridging zone reaches a characteristic, self-similar, length l_{bz}. Numbers refer to stages indicated in the text and **Fig. 8**.

During the first stage, denoted as (1) in **Figs. 8** and **9**, a process zone of length λ^{-1} is created and crack driving force increases until $\mathcal{G}_I = R = \mathcal{G}_{It}$. R is used to denote the resistance of the structure against crack extension which differs from the fracture energy, $\mathcal{G}_{Ic}$, assumed as a material constant under static loading conditions. As expected, the loading kinetic effect is quantitatively not dominating, however non-negligible. However, it is due to the loading kinetic, eq. (13), and the bridging, eq. (17), effects, that the horizontal path, i.e. $\mathcal{G}_I = R$, should not be expected and is replaced by a linearly increasing path – stage (2). The bridging effect, $\mathcal{G}_b^{exp}$, is estimated from experiments as a difference between the analytically obtained ERR, i.e. related to fracture of the epoxy phase, $\mathcal{G}_I$, and the ERR calculated using eq. (3) applied to the experimental force and displacement data. A bridging energy threshold is equated to $\mathcal{G}_{cp} \cong 1\, N/mm$. The corresponding bridging zone spreads over $l_{bz} \cong 20\, mm$, which is found consistent with the macroscopic observations, **Fig**. **6** (**a**). Once the bridging zone is fully developed - l_{bz} becomes constant, a steady-state process is expected – stage (3). Note that due to the loading kinetic effect during stage (3) i.e. $\frac{d\mathcal{G}_{It}}{da} > 0$ the process is stable.

4.2. Discontinuous interface

In **Fig**. **10** the load responses of the specimens with the kissing bond are presented. The experimental and the analytical data are depicted. Confidence bounds, as obtained from the data for specimens without the kissing bond, are used.

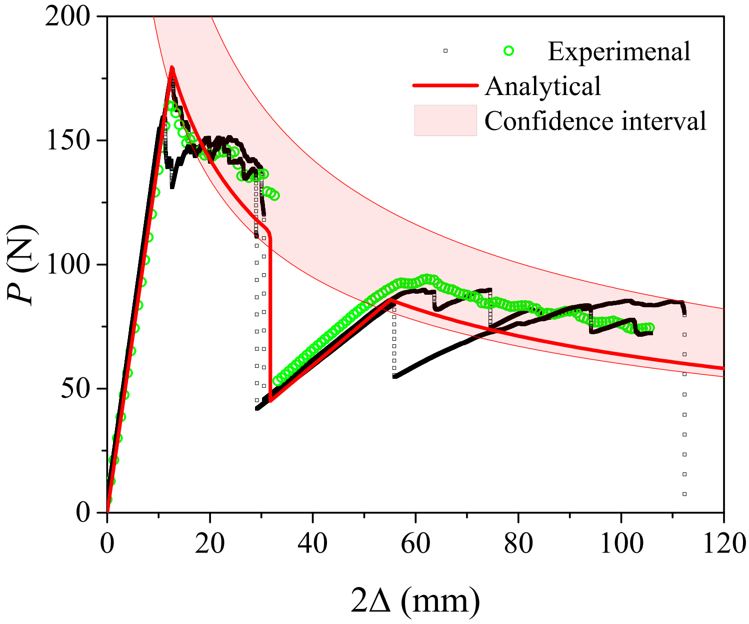

Fig. 10. The load response curves for the specimens with $20\ mm$ kissing bond. The experimental (points) and the analytical (lines) data are plotted with the 95% confidence bounds.

The initial, linear loading path is similar to the specimens without the kissing bond. The loading path bifurcates to the steady-state crack growth stage near the lower bound values. As previously, the load response does not follow the steady-state trend but, instead, rises above it. The situation changes once $2\Delta \cong 30\ mm$. The crack front approaches the kissing bond position. The crack rate increase, $\frac{da}{d\Delta} \rightarrow \infty$, due to the edge effect and, eventually, the crack snaps through the kissing bond to the arrest position, $a \rightarrow a + L_{kiss}$. This process is captured as a snap-down, i.e. $\frac{d\Delta}{dP} = 0$. Subsequently, the loading and the crack initiation stages are repeated followed by a steady-state crack growth process.

4.2.1. Crack locus and crack growth path

In **Fig. 11** a stereoscopic view of the crack growth path of the specimen with the kissing bond is presented.

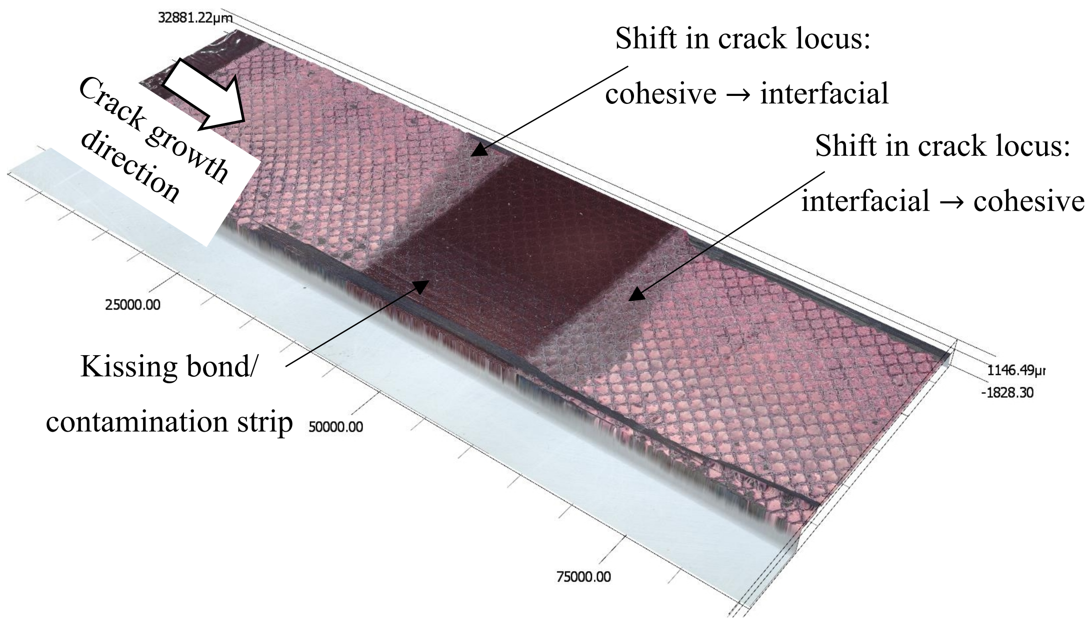

Fig. 11. A 3D image of the fracture surface of one of the adherends with kissing bond along the crack growth path. The scale is given in μm.

The difference between the (strongly) bonded and the kissing bond zones is clearly visible. The strongly bonded zone shares the same features as observed for the 'continuous' specimens. The crack propagated cohesively revealing the characteristic structure of the embedded carrier. Along the kissing bond crack propagated in the adhesive manner – along the composite/adhesive interface. The proximity of the kissing bond zone revealed areas of finite length, indicated by arrows in **Fig**. **11**, that could be related to shift in the crack locus from the cohesive, inside the bondline for the strongly adhering zones, to the interfacial, along the composite/adhesive interface, along the contaminated area. In **Fig**. **12** the height profile of the fracture surface, for arbitrarily chosen line along the crack growth direction, are presented. Specimens with (discontinuous) and without (continuous) kissing bond are compared.

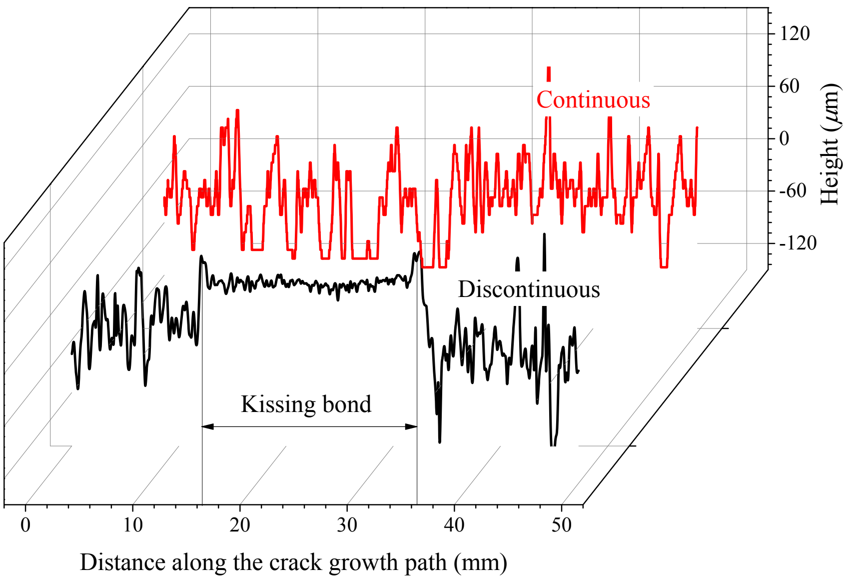

Fig. 12. Comparison of the fracture surface profiles for specimens with and without kissing bond. The profiles were taken along a straight line along the crack growth path.

A difference exists between the cohesive and the adhesive fracture zones. Along the kissing bond a mirror like surface is produced. In contrary, along the cohesive fracture surface, surface profile oscillations become apparent. The arithmetic mean deviation of the profile, i.e. the roughness parameter R_a equates to $\cong 37\ \mu m$ for the cohesive fracture surface, while $R_a \cong 3\ \mu m$ for the kissing bond area. The values express an average from the three specimens with the three height profiles taken from each of specimens along the crack growth direction.

4.2.2. Driving force and resistance curves

In **Fig. 13** the driving force/resistance curves are shown for the discontinuous bondline cases. The experimental and the analytical data are plotted. A grey rectangle is added to denote the size and the position of the kissing bond. Thin, dashed lines represents release of the elastic energy due to the kissing-bond induced snap-down phenomena. The family of curves is then obtained by assuming different values of $\mathcal{G}_{Ic}$ and continuous loading conditions.

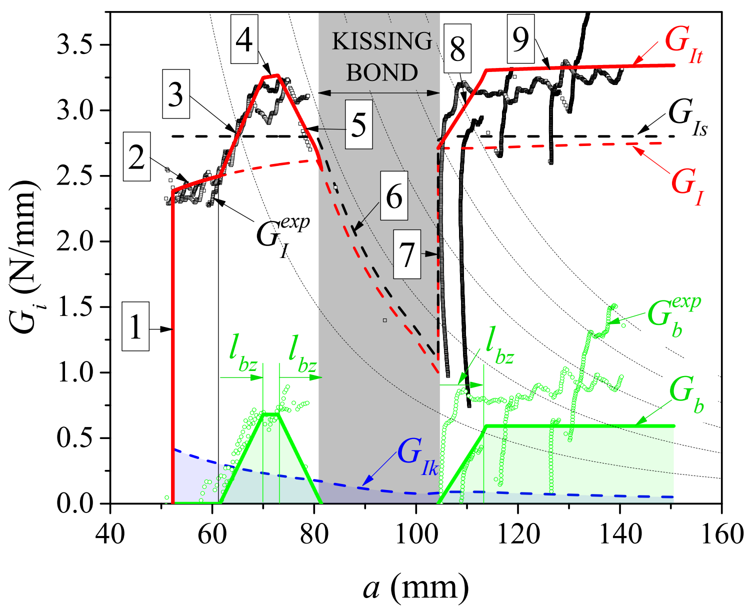

Fig. 13. The driving force/resistance curves for the specimens with a kissing bond along the crack growth path. $\mathcal{G}_I^{exp}$ and $\mathcal{G}_b^{exp}$ represents the total and the bridging component of ERR obtained from the experimental data. The analytical, total ERR $\mathcal{G}_{Itot}$ is composed from static, $\mathcal{G}_{Ist}$, kinetic, $\mathcal{G}_{Ik}$, and bridging, $\mathcal{G}_b$, components. The thin, parallel lines, running from the top to the right of the graph, represent the release of the elastic energy due to the snap-down phenomena.

During loading, stage (1) in **Fig. 13**, the crack driving force increases following a vertical path providing no crack growth occurred. Once the adhesive fracture energy threshold is attained, the crack begins to grow – (2). Note, that contrary to the previous results the bridging does not occurred immediately after onset of the crack and the crack grows following eq. (13), c.f. $\mathcal{G}_I$.

Indeed, the beginning and the end of the bridging process were not controlled. The post-mortem inspection revealed that for the discussed case the carrier remained initially attached to one of the adherends. After ca. 10 mm the cohesive crack growth develops into a process assisted by the bridging – (3). From this stage the fracture process deviates strongly from the one observed for the specimens without the contamination. To facilitate discussion chosen stages of the fracture process are schematically depicted in **Fig. 14** (**a**)-(**d**) with the numbers referring to **Fig. 13**.

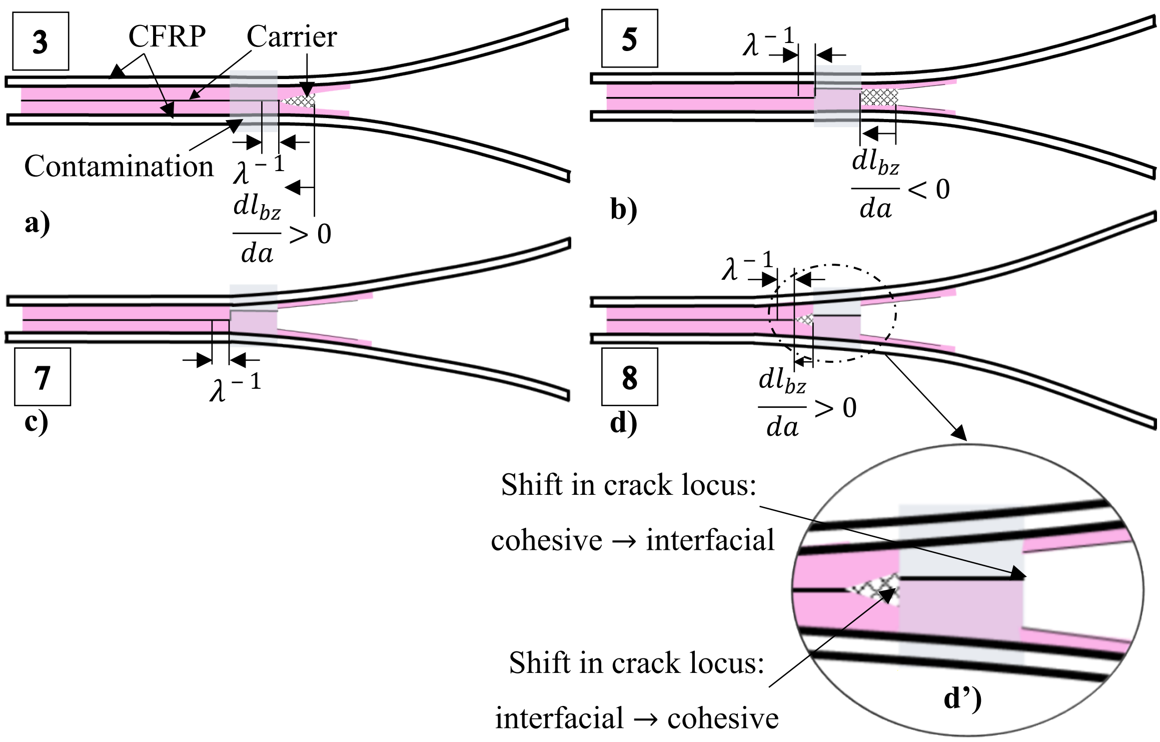

Fig. 14. Chosen aspects of the fracture process of contaminated specimens. (**a**) The build-up of the bridging zone. (**b**) The bridging zone length decreases due to the vicinity of the kissing bond. (**c**) The crack front attains crack arrest position. (**d**) The crack growth from the arrest position incorporating bridging. (**d'**) A detail of (**d**) showing a crack growth path in the vicinity of contamination. Numbers refer to stages indicated in **Fig. 13**.

A similar bridging law is used as for the continuous bondline specimens. However, the length of the bridging zone, as estimated from the experimental data, is now limited to $l_{bz} \cong 7\ mm$ due to the finite size of the bonded zone of ca. 25 mm. Indeed, provided that the crack grew for ca. 10 mm without the bridging, only 15 mm remains for building and diminishing of the bridging zone. An approximately 3 mm transition zone between the increasing and the decreasing stages – (4) is allowed. First, the crack front process zone, defined by λ^{-1}, and later the bridging zone, defined with l_{bz}, are affected by the finite size of the bonded region. While $\lambda^{-1} < l_{bz}$, the process zone is responsible for transferring most of the external loading, i.e. $\mathcal{G}_I > \mathcal{G}_b$. Once attaining the kissing bond position $\frac{dl_{bz}}{da} < 0 \therefore \mathcal{G}_{It} > R \wedge \frac{d\mathcal{G}_{It}}{da} < 0$ - the crack accelerates, viz. (5) and **Fig**. **14** (**b**). Eventually, the load carrying capacity is lost. According to **Fig**. **10**, the snap-down phenomenon takes place with the crack front arresting at the new position denoting the end of the kissing bond, viz. $\frac{d\Delta}{da} = 0 \therefore a \rightarrow a + L_{kiss}$. Since the process is instantaneous (at least in respect to the loading rate, viz. $\dot{a} \gg \dot{\Delta}$) the loading conditions are equivalent to setting $\Delta = const.$ in eqs. (3) and (10). The model follows the force and the displacement data, including the snap-down data from **Fig**. **10**, applied via eq. (3), which are non-zero and continuous along the snap-down owing to the analytical nature of the solution. Consequently, a stable crack driving force equilibrium path - stage (6) in **Fig**. **13**, is obtained. At the crack arrest position, a new loading path nucleates – (7), **Fig**. **14** (**c**). Once $\mathcal{G}_{It} = R$ the loading path bifurcates to the crack growth path but this time the crack growth is assisted by building of the bridging zone – (8), **Fig**. **14** (**d**). As a consequence of a series of events (5) – (8) the crack locus shifts twice as schematically shown in **Fig**. **14** (**d'**) and as implied already from the crack growth path, c.f. **Fig**. **11**. Once the bridging zone is developed the crack begins to propagate in a steady-state manner – (9). It can be observed that one of the curves reaches the level of the specimen without the contamination. On average the effects seem to be smaller. However, at this stage we cannot provide any quantitative reason behind this phenomena. The bridging process was neither designed nor controlled and as such this behaviour could be of stochastic nature. The process described summarizes the main part of the present study. However, during the steady-state process an oscillatory *R* curve character is witnessed, **Figs**. **8** and **13**, which, potentially, makes a steady-state fracture energy an inadequate failure criterion.

5. Oscillating *R* curve: an ad-hoc interpretation of effects due to the carrier lattice structure

5.1. Surface morphology

The primary role of the knitted carrier used within the bondline is to assure a homogeneous and a consistent/reproducible bondline thickness. One of the important findings of the present study reveals a, potentially, huge impact of the carrier on the macroscale fracture resistance. In reality, the presence of the carrier changed the fracture process on both, the macro- and the microscales. The situation depicted in **Fig**. **6** (**a**), i.e. the large-scale bridging must at some stage lead to either ripping/fracture or peeling of the carrier lattice from the adhesive phase and, hence, enhancing the damage tolerance of the joint. In **Fig**. **15** a detailed view of the fracture surface obtained using the 3D scanning technique is presented. In **Fig**. **15** (**a**) a top view is given from which a clear distinction between the carrier and the epoxy adhesive can be made. In **Fig**. **15** (**b**) a schematic representation of the cell structure of the carrier is proposed. **Fig**. **15** (**c**) reveals the complex topography of the fracture surface.

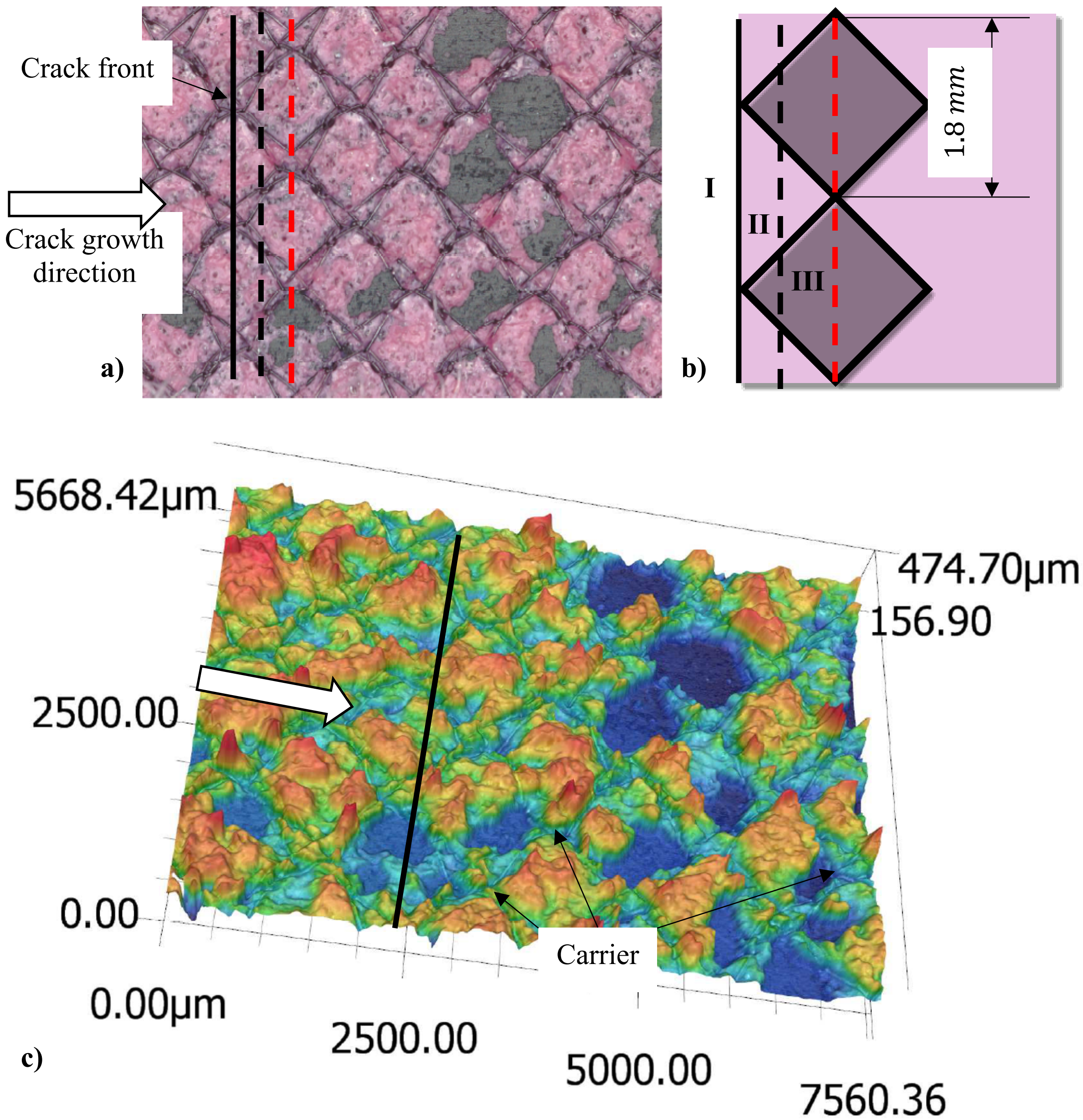

Fig. 15. Details of the crack growth path morphology obtained from 3D scanning. (**a**) Top view of the fracture surface presenting the orientation of the crack front and the propagation direction. (**b**) Simplified representation of the crack growth path and the unit cell structure of the embedded carrier. (**c**) Topography of the crack growth path.

As the available data are unsystematic and due the complexity of processes involved [61-63], which demands a detailed and a separate treatment, a refined quantitative analysis will be pursued in a future study. At present, however, a qualitative explanation will be attempted.

5.2. Peeling of the carrier

Consider a straight front crack propagating through the growth path from position I to position III as schematically presented in **Fig. 15** (**a**) and (**b**). Taking a straight-line cut, the fraction occupied by the adhesive is $f = \frac{l_a}{l_a + l_f}$, with l_a being the line length associated to the adhesive and l_f the length associated to the carrier. In **Fig. 16** (**a**) the height profiles taken along the crack front direction are presented. The results correspond to a single specimen but are representative and reproducible. A thin line illustrates a surface profile along a single, arbitrary path while a bold line is obtained by averaging the height profile along the straight crack front.

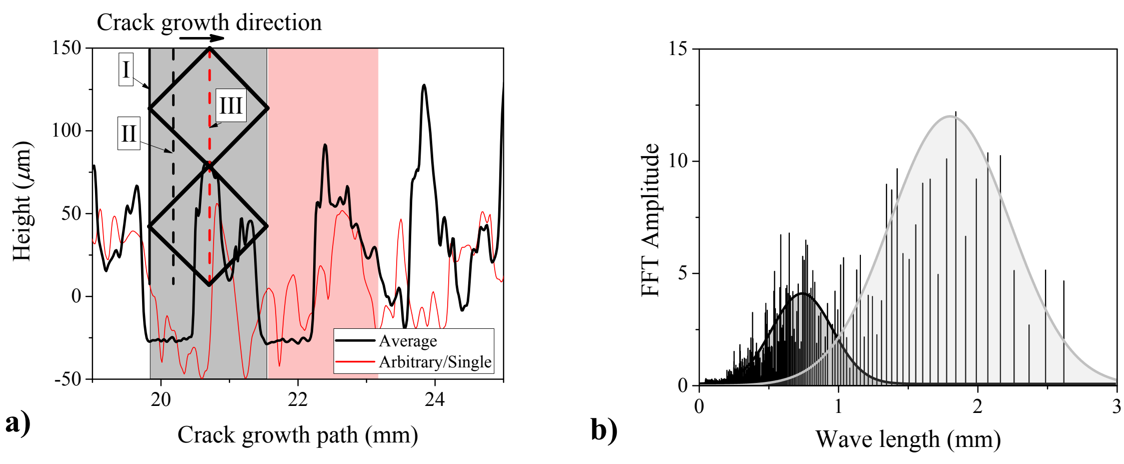

Fig. 16. Surface profiles along the crack front direction. I, II, III refer to the straight crack front position in respect to the lattice grid and consistent with **Fig. 15**.

It is assumed that the minimum observed from the average height profile is expected once the crack front position corresponds to position I in **Fig**. **15** (**b**) (minimum number of knots). For a better illustration, two unit cells of the grid are added to **Fig**. **16** (**a**) with the shaded regions showing the characteristic length of the grid. At this stage a remark must be made that the carrier cells are not always regular nor consistently distributed, c.f. **Fig**. **6** (**b**) and **Fig**. **15** (**a**). A Fast Fourier Transform (FFT) is applied to the profile height for the data gathered along the fracture surface to decide whether or not the periodicity can be associated to the carrier (micro)structure. The results in the form of the FFT amplitude as a function of the wave length are presented in **Fig**. **16** (**b**). Two normal distributions are recognized. The mean wave length of the first distribution yields $0.81\ mm$ while for the second, a value of $1.79\ mm$ is found. This values clearly coincide with the half and the full length of the characteristic dimension of the unit cell. When considering a straight crack front travelling through a single cell upon passing the knot position, viz. I → II, the fraction of the lattice $(1 - f)$ doubles. Subsequently, f remains constant until position III is reached - **Figs**. **15** (**b**) and **16** (**a**). However, providing that the number of cells along the crack front is high enough, ca. 15 cells in the present case, position III can be treated as equivalent to position I. Indeed, the agreement between the reported averaged height profile and the size of the grid appears convincing with the fracture surface experiencing a clear periodicity. To elucidate a possible the effect of composition of the material along the crack front the effective fracture energy of the bondline (omitting the bridging effect) could be defined as [64, 65]:

$$\mathcal{G}_{Ic}^{e} = f\mathcal{G}_{Ia} + (1 - f)\mathcal{G}_{If} \qquad (19)$$

where $\mathcal{G}_{Ia}$ and $\mathcal{G}_{If}$ refer to the fracture energy of the adhesive phase and fracture energy of the interface between the filament and the adhesive. Eq. (20) holds once assuming that the mechanical ERR expressed by components of $\mathcal{G}_I$ coincides with the surface energy following the original assumption of Griffith's fracture theory. From **Fig. 15** (**a**) $f \cong 0.9$ once the straight crack front goes through the knots and $f \cong 0.8$ elsewhere. This agrees with calculations where each arm of the grid is assumed of ca. $2t$ thickness. Substituting such values to eq. (19) shows that oscillations in $\mathcal{G}_I^e$ of order $10^{-2} - 10^{-1}$ could, at least to some extend, be associated with the pattern revealed by the fracture surface. In **Fig. 17** (**a**) the difference between the experimental ERR and the analytical prediction of the fracture energy is given.

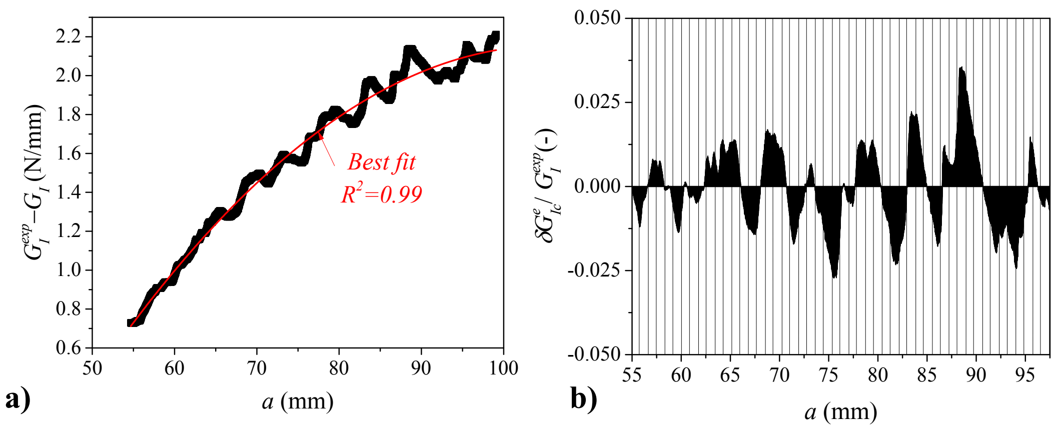

Fig. 17. (**a**) The difference between the experimental and the analytical energy release rate for one of the specimens. (**b**) The normalized residuals of the energy release rate.

Since the bridging and the loading kinetic effects occurred, the data are fitted with the quadratic polynomial function using a least square method to give a trendline and to extract the ERR residuals. In **Fig. 17** (**b**) the ERR residual, i.e. $\delta\mathcal{G}_{Ic}^e = \left(\mathcal{G}_I^{exp} - \mathcal{G}_I\right) - \hat{\mathcal{G}}_I$, with $\hat{\mathcal{G}}_I$ being the expected (statistical) ERR, normalized by the experimental data are presented. Lines with the spacing resembling that of the unit cell are also provided. Once the residuals are plotted against the estimated crack length, a, an oscillating character is revealed. This observation coincides with eq. (19) and can be associated to the lattice-trapping characteristic. The period of the oscillations appears in an encouraging agreement with the size of the cell. However, contrary to eq. (19), which suggests a square wave lattice modulation with a jump at knot positions the experimental data clearly resembles a smoother wave pattern.

5.3. Fracture of the lattice

Following [66] the geometric parameters attributed to the lattice/grid structure are: the shape of the cell – diamond in the present case, the characteristic length of a single cell $l \cong 1.7-2\ mm$ and the shape and the characteristic length scale of the cell wall – thickness/diameter $t \cong 40-50\ \mu m$. From **Fig. 8** we noticed that the growth of the bridging zone, l_{bz}, is altered once $\mathcal{G}_b \cong 1\ N/mm$, which is now assumed to equate to the remote tensile loading (bending and shear contributions should be negligible due to relatively flexible microstructure of the lattice) applied to the lattice material. The calculated fracture stress $\sigma_f \cong 50\ MPa$, using the fraction f as estimated before but with the adhesive being replaced by an hole, seems reasonable and is close to the fracture stress of the epoxy adhesive phase once cured [40]. From an existing study [66] it is recognized that $\sigma_f \propto C\left(\frac{t}{l}\right)^2 \sigma_{TS}$ with $C = const.$ depending on the type of the unit cell and σ_{TS} being the tensile strength of the cell material. Taking $\sigma_{TS} = 800\ MPa$ as an average value for the Nylon material (matweb.com) and equating $\left(\frac{2t}{l}\right)^2 \cong 0.4\ (10^{-3})$ leads to $C \cong 0.4$ which stays in respectable agreement with the results reported for similar lattice systems [66-68]. Once the remote loading achieves σ_f one of the cells breaks. Recalling that the loading conditions do not allow for the snap-back behaviour, therefore the energy released can be attributed to the partial unloading of the otherwise strained lattice structure. Subsequently, the complex composite/adhesive/lattice system is loaded again but in the meantime a new crack surface is created and the bridging zone restored. Leaving limitations of the proposed interpretation (due to e.g. neglecting the local variation in toughness [17, 69, 70], interactions with the remaining length scale parameters of the problem including the effect of the crack front shape [71-73], the adhesive process zone size, the increasing bridging zone size or the straining/restraining of the net material) aside, the deduced sequence explains an oscillating character of events visible in **Fig**. **17**.

5.4. Trapping component of the ERR

The analysis provided indicates a possibility that the oscillating character of the R curve can be induced by the carrier used inside the bondline. To broaden the analysis, due to an apparent similarity between an atomic scale fracture [74, 75] and the structure of the carrier, a lattice model is adopted. The effects mentioned at the end of Section 5.3, i.e. an outcome of the complexity of the material and the process, and standing behind the simplicity of the proposed explanation will lead to the smoothing of a square-wave function given by eq. (19). An empirical, quasi-equilibrium, crack resistance energy function can be introduced:

$$\mathcal{G}^{e}_{Ic} = \mathcal{G}_I + \mathcal{G}_b + \delta\mathcal{G}_L(a)\cos\left(\frac{2\pi l}{a}F^{-1}\right) \tag{20}$$

where $\delta\mathcal{G}_L(a)$ is a modulating trapping component related to the failure of lattice structure of the carrier and F is a function accounting for e.g. effect of the lattice structure inhomogeneity, straining of the lattice etc. As can be observed from **Fig**. **17** (**b**), the amplitude of the normalized ERR, thus $\delta\mathcal{G}_L(a)$, increases during the crack growth. The physical argument being that during the DCB experiment the force, P, decreases, c.f. eq. (4), while fracturing or peeling of an unit cell of the carrier require a critical and constant value of the applied stress/force. The increase in the period of the oscillation, $\sim\left(\frac{l}{a}\right)F$, can be explained using the argument remaining in the spirit of the previous one. Since, viz. eq. (5), $\Delta\sim a^2$ increasing the load to the lattice failure level requires $\frac{da}{d\Delta} > 0$. The oscillating character indicates healing once the crack is trapped by the lattice and coalescing when the crack advances [2, 76]. The normalized lattice trapping component $\delta\mathcal{G}_L(a)\cos\left(\frac{2\pi a}{l}\right)/\mathcal{G}_I^{exp}$ is added to the previous results and shown in **Fig. 18** as a continuous, bold (blue) line.

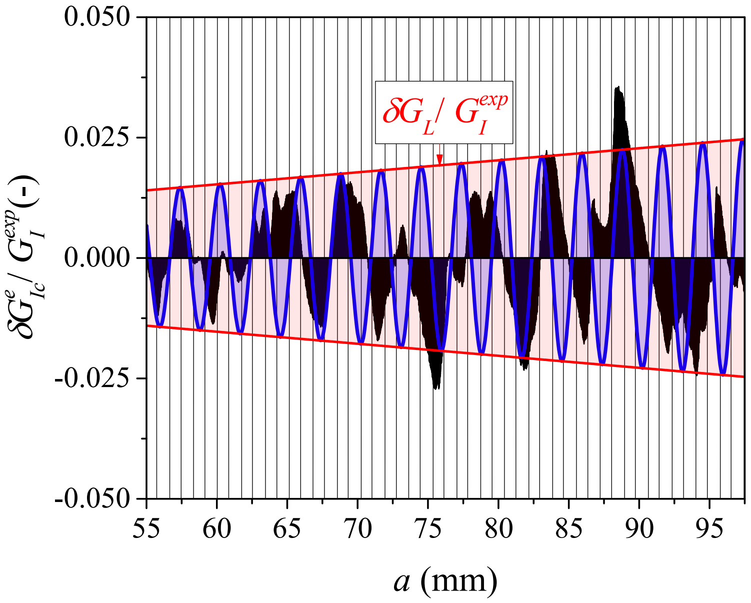

Fig. 18. Oscillating R curve with the lattice trapping component.

Even though a mismatch between the experimental and the analytical data exists the proposed model enables a correct estimation of a crucial lower and upper fracture thresholds. Indeed, eq. (20) exposes the following bounds:

$$\left.\begin{aligned} \mathcal{G}^{e}{}_{Ic}^{+} &= \mathcal{G}_I + \mathcal{G}_b + \delta\mathcal{G}_L(a) \\ \mathcal{G}^{e}{}_{Ic}^{-} &= \mathcal{G}_I + \mathcal{G}_b - \delta\mathcal{G}_L(a) \end{aligned}\right\} \tag{21}$$

which are added to **Fig**. **18** as bold (red) lines. Finally, it can be concluded that although the macroscopic trapping mode is present the macroscopic response of the specimen remains associated mainly to the effective fracture energy of the adhesive.

6. Conclusions

Debonding of composite plates containing kissing bonds along the crack growth path bonded with an epoxy adhesive with a carrier film is investigated experimentally and analytically. The load response data are collected and used to extract fracture properties. A rising R curve behaviour is revealed and associated to the loading kinetic effect and a bridging phenomenon. Contrary to the recognized fibre bridging phenomena expected during the delamination process of Fibre Reinforced Polymers [6, 21, 23, 56, 58], in the present case the bridging is induced by the two-phase composition of the bondline. The macroscopic camera observation reveals that the epoxy adhesive phase plays the role of matrix material for the second phase – 2D lattice material/grid. A significantly increased resistance to fracture of the bonded system is reported. This can be of fundamental importance for designing enhanced fracture toughness and damage tolerance facilitated through bridging of a 2D lattice material. Finally, using 3D fractography the characteristic lattice pattern is recognized on the fracture surface. An efficient analytical model is postulated in which the effects of the loading, the kissing bond and the bridging are incorporated. A complex fracture process is discovered allowing the following conclusions to be drawn.

- The presence of a kissing bond destabilizes the fracture process. In the present case, due to the size of the imperfection, $L_{kiss} > \lambda^{-1}$, the crack propagates in a non-smooth manner.
- The carrier used inside the bondline is found to, effectively, become a second and important phase of the bonding system. Two length scale parameters responsible for transfer of the load between the CFRP plates are recognized: 1) the process zone associated to the epoxy phase and 2) the bridging zone associated with the carrier. Due to the carrier, the resistance to fracture increases significantly by triggering a bridging phenomenon. The topic of using reinforcing materials in the form of lattices inside the adhesive layer can be of an importance for future adhesives with higher resistance to fracture and better damage tolerant. However, this demands further theoretical and experimental investigations.
- The complex fracture process is attempted analytically. The proposed model captures the effect of the loading rate, the kissing bond and uses bridging concept to explain the effect of the lattice/carrier material within the bondline.

Acknowledgments

The authors would like to thank 3M Netherlands B.V. (Netherlands) for suppling the adhesive material.

This work is partly financed by the Netherlands Organisation for Scientific Research (NWO), project number 14366.

References

[1] T.C. Triantafillou, L.J. Gibson, Failure Mode Maps for Foam Core Sandwich Beams, Mater Sci Eng 95 (1987) 37-53.

[2] B.R. Lawn, Fracture of brittle solids, Second edition. ed., Cambridge University Press, Cambridge, 1993.

[3] A. Chambolle, G.A. Francfort, J.J. Marigo, When and how do cracks propagate?, Journal of the Mechanics and Physics of Solids 57(9) (2009) 1614-1622.

[4] D. Leguillon, Strength or toughness? A criterion for crack onset at a notch, Eur J Mech a-Solid 21(1) (2002) 61-72.

[5] N.J. Pagano, Stress Fields in Composite Laminates, International Journal of Solids and Structures 14(5) (1978) 385-400.

[6] Z. Suo, G. Bao, B. Fan, Delamination R-Curve Phenomena Due to Damage, Journal of the Mechanics and Physics of Solids 40(1) (1992) 1-16.

[7] J. Jumel, M.K. Budzik, N. Ben Salem, M.E.R. Shanahan, Instrumented End Notched Flexure - Crack propagation and process zone monitoring. Part I: Modelling and analysis, International Journal of Solids and Structures 50(2) (2013) 297-309.

[8] J. Jumel, N. Ben Salem, M.K. Budzik, M.E.R. Shanahan, Measurement of interface cohesive stresses and strains evolutions with combined mixed mode crack propagation test and Backface Strain Monitoring measurements, International Journal of Solids and Structures 52 (2015) 33-44.

[9] F. Ozdil, L.A. Carlsson, Beam analysis of angle-ply laminate mixed-mode bending specimens, Compos Sci Technol 59(6) (1999) 937-945.

[10] G.I. Barenblatt, Equilibrium Cracks Formed on a Brittle Fracture, Dokl Akad Nauk Sssr+ 127(1) (1959) 47-50.

[11] D.S. Dugdale, Yielding of Steel Sheets Containing Slits, Journal of the Mechanics and Physics of Solids 8(2) (1960) 100-104.

[12] M.F.S.F. de Moura, J.P.M. Goncalves, A.G. Magalhaes, A straightforward method to obtain the cohesive laws of bonded joints under mode I loading, International Journal of Adhesion and Adhesives 39 (2012) 54-59.

[13] H. Khoramishad, M. Hamzenejad, R.S. Ashofteh, Characterizing cohesive zone model using a mixed-mode direct method, Engineering Fracture Mechanics 153 (2016) 175-189.

[14] B.F. Sorensen, E.K. Gamstedt, T.K. Jacobsen, Equivalence of J integral and stress intensity factor approaches for large scale bridging problems, International Journal of Fracture 104(4) (2000) L31-L36.

[15] E.K. Gamstedt, T.K. Jacobsen, B.F. Sorensen, Determination of cohesive laws for materials exhibiting large scale damage zones - From R-Curves for wedge loaded DCB specimens to cohesive laws, Solid Mech Appl 97 (2002) 349-353.

[16] O. Lengline, R. Toussaint, J. Schmittbuhl, J.E. Elkhoury, J.P. Ampuero, K.T. Tallakstad, S. Santucci, K.J. Maloy, Average crack-front velocity during subcritical fracture propagation in a heterogeneous medium, Phys Rev E 84(3) (2011).

[17] L. Legrand, S. Patinet, J.B. Leblond, J. Frelat, V. Lazarus, D. Vandembroucq, Coplanar perturbation of a crack lying on the mid-plane of a plate, International Journal of Fracture 170(1) (2011) 67-82.

[18] K. Kendall, Control of Cracks by Interfaces in Composites, P Roy Soc Lond a Mat 341(1627) (1975) 409-428.

[19] F. Cordisco, P.D. Zavattieri, L.G. Hector, A.F. Bower, On the mechanics of sinusoidal interfaces between dissimilar elastic-plastic solids subject to dominant mode I, Engineering Fracture Mechanics 131 (2014) 38-57.

[20] E. Martin, D. Leguillon, C. Lacroix, A revisited criterion for crack defection at an interface in a brittle bimaterial, Compos Sci Technol 61(12) (2001) 1671-1679.

[21] R.C. Tighe, J.M. Dulieu-Barton, S. Quinn, Identification of kissing defects in adhesive bonds using infrared thermography, International Journal of Adhesion and Adhesives 64 (2016) 168-178.

[22] T. Kundu, A. Maji, T. Ghosh, K. Maslov, Detection of kissing bonds by Lamb waves, Ultrasonics 35(8) (1998) 573-580.

[23] D.W. Yan, B.W. Drinkwater, S.A. Neild, Measurement of the ultrasonic nonlinearity of kissing bonds in adhesive joints, Ndt&E Int 42(5) (2009) 459-466.

[24] M. Perton, A. Blouin, J.P. Monchalin, Adhesive bond testing of carbon-epoxy composites by laser shockwave, J Phys D Appl Phys 44(3) (2011).

[25] C. Jeenjitkaew, F.J. Guild, The analysis of kissing bonds in adhesive joints, International Journal of Adhesion and Adhesives 75 (2017) 101-107.

[26] J.B. Cai, W.Q. Chen, G.R. Ye, Effect of interlaminar bonding imperfections on the behavior of angle-ply laminated cylindrical panels, Compos Sci Technol 64(12) (2004) 1753-1762.

[27] R. Alvarez-Lima, A. Diaz-Diaz, J.F. Caron, S. Chataigner, Enhanced layerwise model for laminates with imperfect interfaces - Part 1: Equations and theoretical validation, Compos Struct 94(5) (2012) 1694-1702.

[28] K. Matous, M.G. Kulkarni, P.H. Geubelle, Multiscale cohesive failure modeling of heterogeneous adhesives, Journal of the Mechanics and Physics of Solids 56(4) (2008) 1511-1533.

[29] A. Needleman, An Analysis of Decohesion Along an Imperfect Interface, International Journal of Fracture 42(1) (1990) 21-40.

[30] P. Feraren, H.M. Jensen, Cohesive zone modelling of interface fracture near flaws in adhesive joints, Engineering Fracture Mechanics 71(15) (2004) 2125-2142.

[31] H. Gao, J.R. Rice, A First-Order Perturbation Analysis of Crack Trapping by Arrays of Obstacles, Journal of Applied Mechanics 11 (1989) 828-836.

[32] M.K. Budzik, H.M. Jensen, Perturbation analysis of crack front in simple cantilever plate peeling experiment, International Journal of Adhesion and Adhesives 53 (2014) 29-33.

[33] M. Vasoya, V. Lazarus, L. Ponson, Bridging micro to macroscale fracture properties in highly heterogeneous brittle solids: weak pinning versus fingering, Journal of the Mechanics and Physics of Solids 95 (2016) 755-773.

[34] V. Lazarus, Perturbation approaches of a planar crack in linear elastic fracture mechanics: A review, Journal of the Mechanics and Physics of Solids 59(2) (2011) 121-144.

[35] M. Vasoya, A.B. Unni, J.B. Leblond, V. Lazarus, L. Ponson, Finite size and geometrical non-linear effects during crack pinning by heterogeneities: An analytical and experimental study, Journal of the Mechanics and Physics of Solids 89 (2016) 211-230.

[36] V. Lazarus, J.B. Leblond, In-plane perturbation of the tunnel-crack under shear loading I: bifurcation and stability of the straight configuration of the front, International Journal of Solids and Structures 39(17) (2002) 4421-4436.

[37] V. Tvergaard, J.W. Hutchinson, Analyses of crack growth along interface of patterned wafer-level Cu-Cu bonds, International Journal of Solids and Structures 46(18-19) (2009) 3433-3440.

[38] C. Cuminatto, G. Parry, M. Braccini, A model for patterned interfaces debonding - Application to adhesion tests, International Journal of Solids and Structures 75-76 (2015) 122-133.

[39] S. Heide-Jorgensen, M.K. Budzik, Crack growth along heterogeneous interface during the DCB experiment, International Journal of Solids and Structures 120 (2017) 278-291.

[40] S.T. Freitas, J. Sinke, Failure analysis of adhesively-bonded metal-skin-to-composite-stiffener: Effect of temperature and cyclic loading, Compos Struct 166 (2017) 27-37.
[41] P. Limited, 2017. http://www.paintservices.com/pf-qd/. 2017).
[42] J.A. Poulis, J.C. Cool, E.H.P. Logtenberg, Uv/Ozone Cleaning, a Convenient Alternative for High-Quality Bonding Preparation, International Journal of Adhesion and Adhesives 13(2) (1993) 89-96.
[43] R. Oosterom, T.J. Ahmed, J.A. Poulis, H.E.N. Bersee, Adhesion performance of UHMWPE after different surface modification techniques, Med Eng Phys 28(4) (2006) 323-330.
[44] S.T. de Freitas, M.D. Banea, S. Budhe, S. de Barros, Interface adhesion assessment of composite-to-metal bonded joints under salt spray conditions using peel tests, Compos Struct 164 (2017) 68-75.
[45] J.A. Poulis, Small Cylindrical Adhesive Bonds, Technical University Delft, The Netherlands, 1993.
[46] S.T. de Freitas, D. Zarouchas, H. Poulis, The Use Of Acoustic Emission And Composite Peel Tests To Detect Weak Adhesion In Composite Structures, The Journal of Adhesion.
[47] J.N. Reddy, Mechanics of laminated composite plates and shells : theory and analysis, 2nd ed., CRC Press, Boca Raton, 2004.
[48] A.A. Griffith, The phenomena of rupture and flow in solids, Philosophical Transactions of the Royal Society of London A 221 (1921) 163-198.
[49] P. Davidson, A.M. Waas, Non-smooth mode I fracture of fibre-reinforced composites: an experimental, numerical and analytical study, Phil. Trans. R. Soc. A 370 (2012) 1942–1965.
[50] A. Okada, I.N. Dyson, A.J. Kinloch, Subcritical Interlaminar Crack-Growth in Fiber Composites Exhibiting a Rising R-Curve, J Mater Sci 30(9) (1995) 2305-2312.
[51] D. Sen, M.J. Buehler, Structural hierarchies define toughness and defect-tolerance despite simple and mechanically inferior brittle building blocks, Sci Rep-Uk 1 (2011).
[52] M.F. Kanninen, Dynamic Analysis of Unstable Crack-Propagation and Arrest in Dcb Test Specimen, International Journal of Fracture 10(3) (1974) 415-430.
[53] M. Cabello, J. Zurbitu, J. Renart, A. Turon, F. Martínez, A general analytical model based on elastic foundation beam theory for adhesively bonded DCB joints either with flexible or rigid adhesives, International Journal of Solids and Structures 94-95 (2016) 21-34.
[54] S. Krenk, Energy-Release Rate of Symmetrical Adhesive Joints, Engineering Fracture Mechanics 43(4) (1992) 549-559.
[55] M.K. Budzik, J. Jumel, M.E.R. Shanahan, An in situ technique for the assessment of adhesive properties of a joint under load, International Journal of Fracture 171(2) (2011) 111-124.
[56] M.M. Shokrieh, M. Salamat-talab, M. Heidari-Rarani, Dependency of bridging traction of DCB composite specimen on interface fiber angle, Theor Appl Fract Mec 90 (2017) 22-32.
[57] S.P. Fernberg, L.A. Berglund, Bridging law and toughness characterisation of CSM and SMC composites, Compos Sci Technol 61(16) (2001) 2445-2454.
[58] B.F. Sorensen, T.K. Jacobsen, Large-scale bridging in composites: R-curves and bridging laws, Compos Part a-Appl S 29(11) (1998) 1443-1451.
[59] A.J. Brunner, B.R.K. Blackman, J.G. Williams, Calculating a damage parameter and bridging stress from G(IC) delamination tests on fibre composites, Compos Sci Technol 66(6) (2006) 785-795.
[60] M.F. Kanninen, Augmented Double Cantilever Beam Model for Studying Crack-Propagation and Arrest, International Journal of Fracture 9(1) (1973) 83-92.
[61] I. Quintana-Alonso, N.A. Fleck, Damage Tolerance of a Sandwich Panel Containing a Cracked Square Lattice Core, J Sandw Struct Mater 12(2) (2010) 139-158.

[62] I. Quintana-Alonso, S.P. Mai, N.A. Fleck, D.C.H. Oakes, M.V. Twigg, The fracture toughness of a cordierite square lattice, Acta Materialia 58(1) (2010) 201-207.
[63] X.D. Cui, Z.Y. Xue, Y.M. Pei, D.N. Fang, Preliminary study on ductile fracture of imperfect lattice materials, International Journal of Solids and Structures 48(25-26) (2011) 3453-3461.
[64] R. Tadepalli, K.T. Turner, C.V. Thompson, Mixed-mode interface toughness of wafer-level Cu–Cu bonds using asymmetric chevron test, Journal of the Mechanics and Physics of Solids 56 (2008) 707–718.
[65] R. Tadepalli, T.K. Turner, C.V. Thompson, Effects of patterning on the interface toughness of wafer-level Cu–Cu bonds, Acta Materialia 56(3) (2008) 438-447.
[66] L.J. Gibson, M.F. Ashby, Cellular solids : structure and properties, Nota, Kbh., 2016.
[67] I.Q. Alonso, N.A. Fleck, Compressive response of a sandwich plate containing a cracked diamond-celled lattice, Journal of the Mechanics and Physics of Solids 57(9) (2009) 1545-1567.
[68] F. Lipperman, M. Ryvkin, M.B. Fuchs, Fracture toughness of two-dimensional cellular material with periodic microstructure, International Journal of Fracture 146(4) (2007) 279-290.
[69] S. Patinet, D. Vandembroucq, A. Hansen, S. Roux, Cracks in random brittle solids: From fiber bundles to continuum mechanics, Eur Phys J-Spec Top 223(11) (2014) 2339-2351.
[70] S. Patinet, D. Vandembroucq, S. Roux, Quantitative Prediction of Effective Toughness at Random Heterogeneous Interfaces, Physical Review Letters 110(16) (2013).
[71] M.K. Budzik, J. Jumel, M.E.R. Shanahan, On the crack front curvature in bonded joints, Theor Appl Fract Mec 59(1) (2012) 8-20.
[72] K.F. Nilsson, On Growth of Crack Fronts in the Dcb-Test, Compos Eng 3(6) (1993) 527-546.
[73] L.J. Yu, B.D. Davidson, A three-dimensional crack tip element for energy release rate determination in layered elastic structures, J Compos Mater 35(6) (2001) 457-488.
[74] R. Thomson, C. Hsieh, V. Rana, Lattice Trapping of Fracture Cracks, J Appl Phys 42(8) (1971) 3154-&.
[75] R. Thomson, Pinning of Cracks by Dislocations, B Am Phys Soc 18(3) (1973) 394-394.
[76] D. Maugis, Sub-Critical Crack Growth, Surface Energy and Fracture Toughness of Brittle Materials, in: E.A.G. Bradt R.C., Hasselman D.P.H., Lange F.F. (Ed.) Fracture Mechanics of Ceramics, Springer, Boston, MA, 1986.